

An experimental study of electro-osmotic flow in rectangular microchannels

By R. SADR¹, M. YODA¹†, Z. ZHENG² AND A. T. CONLISK³

¹G. Woodruff School of Mechanical Engineering, Georgia Institute of Technology, Atlanta, GA 30332-0405, USA

²Biomedical Engineering Center, The Ohio State University, Columbus, OH 43210, USA

³Department of Mechanical Engineering, The Ohio State University, Columbus, OH 43210, USA

(Received 27 August 2003 and in revised form 21 February 2004)

Experimental studies were carried out on fully developed and steady electro-osmotic flow in a rectangular channel where the channel height h is comparable to its width and the thickness of the electric double layer characterized by the Debye length is much less than h . The nano-particle image velocimetry technique was used to measure the two components of the velocity field parallel to and within about 100 nm of the channel wall for $h \leq 25 \mu\text{m}$. The mobility of the particle tracers was calculated from averaged velocity data for various electric field strengths. The experimentally determined mobility values are compared with analytical predictions for dilute aqueous solutions of sodium tetraborate.

1. Introduction

Electro-osmotic flow (EOF) is by definition the flow of an electrolyte solution driven by an external electric field through a channel with charged walls. The surface charge is created in this case by adsorption of ions from the electrolyte solution onto the channel walls. We consider EOF through rectangular microchannels with dimensions along the (x, y, z) axes of (L, h, W) , respectively, where x is the streamwise direction, y is the direction normal to the wall, and z is the direction along the channel wall of interest normal to x . In the cases studied here, the channel height and width are comparable, or $h/W = O(1)$, and the flow is fully developed, with $h/L \ll 1$. The charged channel walls attract free ions of the opposite sign from the electrolyte solution to create an electric double layer (EDL), whose thickness is the Debye (screening) length λ , typically $O(0.1 \text{ nm} - 10 \text{ nm})$ for aqueous solutions at molar concentrations $C = O(1 \text{ M} - 10^{-4} \text{ M})$, respectively. The difference in potential across the EDL, or between the charged wall and the bulk electrolyte solution, is known as the wall ζ -potential. Outside the EDL, the velocity profile in electro-osmotic flow is uniform. The electro-osmotic mobility μ_{eo} is defined as the bulk electro-osmotic speed divided by the driving electric field E .

Electrokinetic ‘pumping’ is the leading technology for driving flows through microchannels, especially for channels where $h < O(10 \mu\text{m})$, because EOF can achieve much higher volumetric flow rates Q than pressure gradient-driven flow. In fully developed EOF, $Q \propto h$ for a given E ; in Poiseuille flow, $Q \propto h^3$ for a given pressure gradient. Electrokinetic pumping is also the leading technology for biochemical

† Author to whom correspondence should be addressed: minami.yoda@me.gatech.edu

separations at the microscale, since the (nearly) uniform velocity profiles of EOF result in much less Taylor dispersion than Poiseuille flow. Taylor dispersion is a major limitation for compact biochemical separations using 'lab on a chip' devices since efficient separation of large biomolecules requires high sample concentrations (Culbertson, Jacobson & Ramsey 1998; Vazquez *et al.* 2002).

There are numerous analytical and numerical studies of fully developed and steady EOF in parallel-plate, rectangular and round geometries (Rice & Whitehead 1965; Levine, Marriott & Robinson 1975; Hunter 1981; Probst 1989; Yang, Li & Masliyah 1998; among others). Ghosal (2002) used a lubrication approximation to investigate the effects of slowly varying cross-section geometry and wall charge on EOF in a microchannel, and concluded that the pressure gradient introduced by variations in cross-section geometry increased Taylor dispersion. Fu, Lin & Yang (2003) showed that a sudden step change in the wall ζ -potential had a major impact on the velocity and pressure profiles in parallel-plate EOF. Almost all of these studies use the classical Debye–Hückel linear approximation of the Poisson–Boltzmann equation and/or assume that the flow is symmetric about the centreline of the channel. An exception is the work of Conlisk *et al.* (2000), who considered EOF of two ionic species in both parallel-plate and rectangular micro- and nanochannels and obtained numerical results for velocity, potential and species mole fractions. The numerical results were in excellent agreement with analytical results obtained with a singular perturbation analysis in the limit of $\lambda \ll h$ and experimental measurements of volumetric flowrate. In related work, Zheng, Hansford & Conlisk (2003) considered the effect of multivalent ionic species on ionic transport; their results compare well with experimental data. The results of Conlisk *et al.* (2002) and Zheng *et al.* (2003) are in agreement with the classical models of electro-osmotic flow cited above.

However, there are relatively few experimental (*vs.* analytical and numerical) studies of electro-osmotic flow in microchannels. The bulk of the experimental work on EOF in microchannels has focused upon quantifying separation and concentration in capillary electrophoresis using global flowrate and mobility measurements (for example, Jacobson *et al.* 1994a; Vazquez *et al.* 2002; Broyles, Jacobson & Ramsey 2003). We know of only three studies that have obtained velocity profiles in EOF through microchannels. Paul, Garguilo & Rakestraw (1998) used scalar imaging velocimetry of a caged rhodamine dye to obtain radial velocity profiles in electrokinetically driven flow through open 75 μm and 100 μm fused silica capillaries with an out-of-plane spatial resolution of about 20 μm . They reported discrepancies in their velocity results near the charged walls of the capillary, and suggested that this was due to electrophoresis of their charged (uncaged) tracer. Herr *et al.* (2000) used a similar technique to determine radial velocity profiles in 75 μm diameter fused silica capillaries whose inner walls were partially coated with an EOF-suppressing polymer to create a sudden step change in the wall ζ -potential. Finally, Cummings (2002) reported micro-particle image velocimetry (μPIV) measurements using fluorescent 200 nm latex spheres in EOF between parallel plates spaced 10 μm apart by periodic arrays of square and circular posts.

Although spatially and temporally resolved experimental data are required to validate existing analytical and numerical models of electrokinetically driven transport at the micro- and nanoscale, experimental studies at these scales are at present greatly limited by the lack of measurement techniques with appropriate spatial resolution. At present, the most common technique for measuring velocities in microchannels, μPIV (Santiago *et al.* 1998), can obtain measurements no closer than 450 nm from the

wall (Tretheway & Meinhart 2002) with an out-of-plane spatial resolution, at best, of 2–6 μm (Santiago *et al.* 1998; Stone, Meinhart & Wereley 2002).

We have developed over the last few years a complementary velocimetry technique, nano-PIV (nPIV) (Zettner & Yoda 2003) uniquely suited to near-wall velocity measurements in micro- and nanochannels. Nano-PIV obtains nearly instantaneous measurements of two components of the flow velocity by determining the displacement over time of neutrally buoyant particle tracers as they are convected by the flow. The technique differs from μPIV in its use of evanescent-wave (*vs.* volume) illumination. An evanescent wave is generated by the total internal reflection (TIR) of light at the interface between two materials with different refractive indices n_1 and n_2 ($n_1 < n_2$). The evanescent wave propagates parallel to the interface in the lower refractive index medium with an intensity \mathcal{I} that decays exponentially with distance normal to the interface y (Axelrod, Burghardt & Thompson 1984; Prieve & Frej 1990):

$$\frac{\mathcal{I}}{\mathcal{I}_0} = \exp\left\{-\frac{y}{y_p}\right\} \quad \text{where} \quad y_p = \frac{\lambda_0}{4\pi} [n_2^2 \sin^2 \theta - n_1^2]^{-1/2}. \quad (1.1)$$

Here, \mathcal{I}_0 is the light intensity at the interface ($y=0$), y_p is the penetration depth, λ_0 is the wavelength of the illumination in vacuum, and θ is the angle of incidence.

Because PIV typically interrogates a thin plane of the flow, two different spatial resolutions must be considered in these techniques, namely the ‘out-of-plane’ spatial resolution, or the resolution along the direction normal to the image plane, and the ‘in-plane’ spatial resolution, or that within the image plane. In nPIV, the out-of-plane spatial resolution along the y -direction is determined by the greater of two experimental parameters: the thickness of the evanescent wave, of $O(y_p)$, or the tracer particle diameter D . In μPIV , the out-of-plane spatial resolution is related to the depth of field of the imaging optics, typically of $O(1\ \mu\text{m})$, and the spatial extent of the illumination source is much greater than this depth of field. Because the illumination used for μPIV interrogates a region well beyond this depth of field, however, light from the tracers that sample the flow beyond this depth of field are also imaged. This out-of-focus light reduces the SNR and the accuracy of μPIV (Meinhart, Wereley & Gray 2000), and suggests that the out-of-plane spatial resolution of μPIV exceeds the depth of field. Although various techniques such as cross-correlation averaging have greatly improved the in-plane spatial resolution of μPIV (Meinhart, Wereley & Santiago 2000), we are unaware of any techniques that reduce the out-of-plane spatial resolution of this technique.

Nano-PIV is therefore a technique that has an out-of-plane spatial resolution that is at least an order of magnitude smaller than μPIV and – since techniques such as cross-correlation averaging are applicable to both nPIV and μPIV – an in-plane spatial resolution comparable to that of μPIV . As such, this new technique is uniquely suited to obtaining near-wall velocity data in flows where the velocity varies significantly over lengthscales below $O(1\ \mu\text{m})$ normal to the wall.

Nano-PIV was used in these initial studies to obtain velocity data in fully developed and steady EOF through rectangular quartz microchannels with a minimum dimension $h \leq 25\ \mu\text{m}$ within 90–110 nm of the wall with an out-of-plane spatial resolution of 100 nm. The nPIV tracer particles are subject to both EOF and, if charged, electrophoresis. The experimentally derived mobility μ_{ex} is defined as the particle speed in the bulk flow due to both EOF and electrophoresis divided by the driving electric field.

Section 2 details with the experimental measurements in rectangular fused silica microchannels using the nPIV technique. Section 3 gives velocity field data from

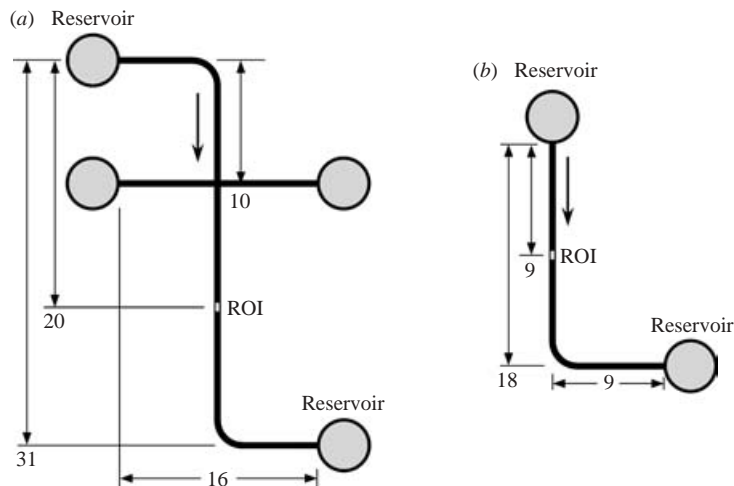
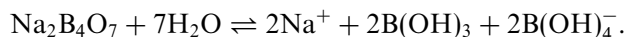


FIGURE 1. Top view of the (a) cross and (b) single channel chips used in these studies with nominal dimensions given in mm. The region of interest (ROI) is indicated by the white region. Flow goes from top to bottom, as shown by the arrow.

the experiments at different ionic strengths and electric fields. The mobility of the particle tracers is determined from the slope of these velocity data and compared with analytical predictions for electro-osmotic mobility from the model of Conlisk *et al.* (2002).

2. Experimental description

EOF of dilute aqueous solutions of the weak base sodium tetraborate ($\text{Na}_2\text{B}_4\text{O}_7$), or borax, at molar concentrations $C = 0.19 - 36 \text{ mM}$ driven by a steady electric field $E = 0 - 4.8 \text{ kV m}^{-1}$ was studied in rectangular microchannels with cross-sectional dimensions $h \times W$. At these concentrations, the borax dissociates in aqueous solution to give anion and cation species with a valence of unity:



The ionic strength I ($I \equiv \sum_{i=1}^N z_i^2 c_i$, where z_i and c_i are the valence and molar concentration of the i th ionic species, respectively) of the solution is then twice the concentration.

Figure 1 depicts the fused silica, or quartz, microchannel chips used in these experiments. Two different chip geometries were used here: (a) a cross with two intersecting microchannels for $C = 1.9, 3.6$ and 36 mM ; and (b) a single channel with one 90° bend for $C = 0.19$ and 18.4 mM . All channel cross-sectional dimensions are given in table 1. The chips were fabricated by the group of J.M. Ramsey in the Chemical Sciences Division at Oak Ridge National Laboratories using standard photolithography followed by chemical wet etching of $50 \text{ mm} \times 25 \text{ mm}$ (nominal dimensions) pieces of fused silica with a thickness of 1 mm for all cases except for the chip used for $C = 0.19 \text{ mM}$, where a 2 mm thick piece was used (Jacobson *et al.* 1994b). The chemical wet etch process produces a roughly trapezoidal cross-section; h is therefore the depth of the etch and W is defined as the width at half-depth. The trapezoidal open channel is then sealed on the bottom by a 1 mm thick fused silica cover slip using a high-temperature bonding technique (Jacobson *et al.* 1994b).

C (mM)	I (mM)	h (μm)	W (μm)	Chip type	λ (nm)	ϕ (%)
0.19	0.38	4.9	17.3	<i>b</i>	8.8	0.09
1.9	3.8	10.2	26.1	<i>a</i>	5.0	0.07
3.6	7.2	24.7	51.2	<i>a</i>	4.0	0.1
18.4	36.8	4.8	17.9	<i>b</i>	2.0	0.08
36	72	24.7	51.2	<i>a</i>	1.5	0.1

TABLE 1. Summary of experimental parameters for the five different cases.

The channel wall of interest in these measurements was taken in all cases to be the cover slip surface with a surface roughness of $O(1\text{ nm})$; the wet etch process gives a surface roughness for the other three walls of the microchannel of $O(10\text{ nm})$. The region of the microchannel imaged in these experiments was at least $360h$ downstream of any bends or intersections to ensure fully developed flow. Experiments were carried out in the cross-microchannel geometries with both ‘forwards’ and ‘backwards’ flow (i.e. top to bottom and bottom to top, respectively, in figure 1*a*) to verify that the cross-intersection had no effect on the data.

Holes were ultrasonically drilled through the cover slip to the circular wells etched into the chip. Reservoirs consisting of 12.7 mm lengths (nominal dimensions) of borosilicate glass tubing with an inner diameter of 3.8 mm were bonded to the wells and the cover slip through-holes using a high-temperature two-component optical epoxy (EPO-TEK 353ND-T) for all cases except $C = 0.19\text{ mM}$, where only two reservoirs consisting of 6.3 mm lengths of 2.9 mm i.d. borosilicate tubing were attached to the upstream and downstream ends of the long channel (the vertical channel in figure 1*a*). The location of the reservoirs varied by up to 1 mm owing to uncertainties associated with the positions of the through-holes.

The reservoirs at the ends of the ‘vertical’ microchannel (cf. figure 1) were filled with about 0.15 ml (0.04 ml for $C = 0.19\text{ mM}$) of a buffer consisting of sodium tetraborate decahydrate salt ($\text{Na}_2\text{B}_4\text{O}_7 \cdot 10\text{H}_2\text{O}$) (ACS reagent grade, Acros Organics) dissolved in Nanopure water. Fluorescent polystyrene spheres of $D = 100\text{ nm}$ (Estapor XC, Bangs Laboratories) were added to this solution at volume fractions $\phi = 0.07\text{--}0.1\%$ (cf. table 1) as the tracers. The fluorescent tracer particles have excitation and emission maxima at 480 nm and 520 nm, respectively, and a density of 1.05 g cm^{-3} . A d.c. power supply (Agilent E3612A) connected to platinum electrodes immersed in the two reservoirs at the ends of the vertical microchannel was used to impose the electric field. In all cases, the microchannel was allowed to sit for several minutes after the reservoirs were filled to ensure that the upstream and downstream reservoir free surfaces were at the same altitude and there was no net flow before imposing an electric field.

In these experiments, the chips were mounted horizontally on a microscope stage. A $\lambda_0 = 488\text{ nm}$ argon-ion laser (Coherent Innova 90) beam with an output power of 0.1 W was focused at an angle with respect to the normal of about 40° on to one of the legs of an isosceles right-angled triangle prism of fused silica ($n = 1.46$) whose hypotenuse is optically coupled with glycerine to the upper surface of the microchannel chip (figure 2). This beam is refracted through the prism and the entire thickness of the chip, and then undergoes TIR with an angle of incidence $\theta \approx 70^\circ$ at the quartz–water interface at the top of the cover slip comprising the bottom wall of the microchannel. The evanescent waves that are imaged here are from the first or second TIR at the top of the cover slip. Since the refractive indices of water

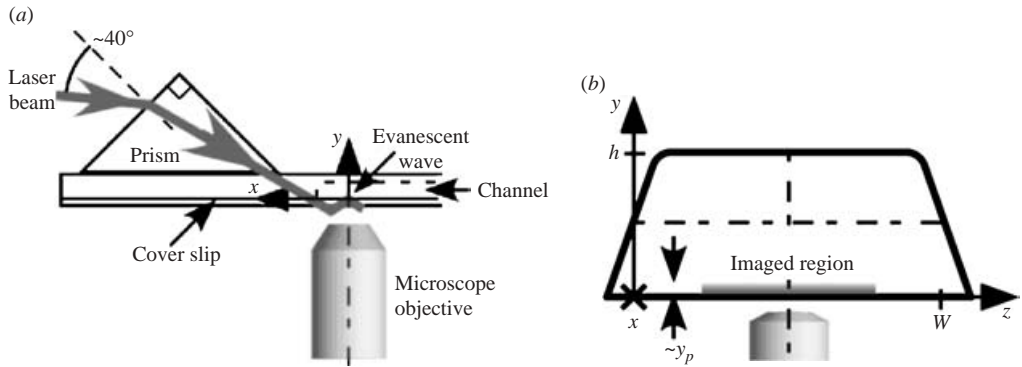


FIGURE 2. Sketch of (a) the evanescent-wave illumination and imaging setup and (b) channel cross-section. Only the bottom part of the microchannel (i.e. the region near the downstream reservoir) is shown in (a).

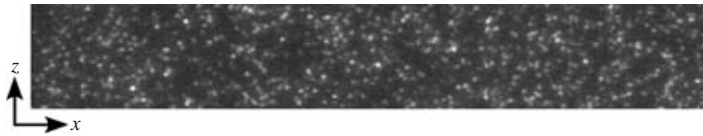


FIGURE 3. Typical image (exposure 1 ms) of 100 nm particle tracers in EOF of $C = 3.6$ mM sodium tetraborate at $E = 1.0$ kV m⁻¹. The field of view is 110 μ m (x) by 16 μ m (z).

and quartz are $n_1 = 1.33$ and $n_2 = 1.46$, (1.1) gives $y_p = 90 - 110$ nm. This penetration depth determines the out-of-plane spatial resolution of the nPIV technique.

The region illuminated by the evanescent wave is next to the cover slip at the bottom of the channel to minimize surface roughness and in the centre of the channel to minimize edge effects. The fluorescent particle tracers are viewed through an inverted epi-fluorescent microscope (Leica DMIRE2) adapted for evanescent-wave illumination from the TIR of a laser beam through a 63×0.5 objective (Leica PL Fluotar L). A dichroic beamsplitter cube (Leica I3) in the microscope separates the longer-wavelength fluorescence from the evanescent wave illumination so that only the fluorescence from the particles is imaged by the microscope. The fluorescence from the particle tracers are acquired as 100 row \times 653 column images on a CCD camera with on-chip gain (Photometrics Cascade 650) at framing rates of 160 Hz with 1 ms exposure. Figure 3 shows a typical raw image. Up to 1000 consecutive images are written in real-time on to the HD on a PC.

With this imaging system, a 100 nm fluorescent particle illuminated by the evanescent wave spans 7–8 pixels owing to diffraction effects (Crocker & Grier 1996). Particles closer to the wall within the evanescent-wave layer are illuminated with a higher light intensity and hence have larger images. The large particle image size imposes an upper limit upon the tracer volume fraction ϕ of about 0.25%.

The EdPIV software of Wereley, Gui & Meinhart (2002) was used to determine the particle (and presumably flow) velocities. The analysis program correlates two interrogation windows using a FFT-based cross-correlation with typical dimensions of 110 pixels \times 80 pixels ($x \times z$), corresponding to in-plane spatial resolutions of about 18 μ m and 13 μ m along x and z , respectively. The location of the cross-correlation peak was determined using a three-point Gaussian peak-fit along the x - and z -directions. There was 50% overlap between adjacent windows, giving 18 particle displacement

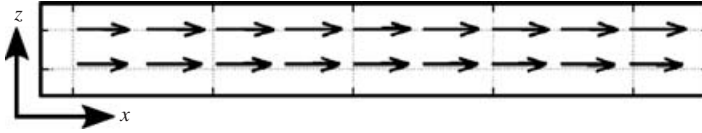


FIGURE 4. Temporally averaged nPIV result for EOF of $C = 3.6$ mM sodium tetraborate at $E = 1.0 \text{ kV m}^{-1}$. These vectors represent a spatially averaged velocity $U = 17.6 \text{ } \mu\text{m s}^{-1}$.

vectors for each image. No window shift is used between the first and second images within the pair, since the displacement within the pair is typically less than 3 pixels.

These relatively large interrogation windows were chosen to minimize the standard deviation in the results, and ensure that the number of particle images in each window is large enough (typically at least 30) to ensure a cross-correlation peak with a good signal to noise ratio (Keane & Adrian 1991), even with significant particle mismatch between two successive exposures owing to Brownian diffusion. Although techniques such as cross-correlation averaging can be used with these data to improve the in-plane spatial resolution with the ultimate limit determined by the tracer size, these techniques were not used here since this flow was uniform in x and z and since estimates of the errors due to both tangential (i.e. in-plane) and normal (i.e. out-of-plane) Brownian diffusion could be obtained from these temporally resolved results. Smaller window sizes and cross-correlation averaging were tested upon a subset of the nPIV images, and gave results similar to those reported here.

In the cases studied here, the flow is essentially also uniform in y , since the EDL should occupy a small fraction of the out-of-plane spatial resolution. In all cases, λ is predicted to be less than 9 nm (Zheng *et al.* 2003), *vs.* a penetration depth $y_p = 90\text{--}110$ nm (table 1). Note that these predictions are based upon the mole fractions of the cation and anion at the wall (*vs.* the reservoir concentration, which is usually the case) calculated iteratively using an equilibrium argument from the electrolyte concentrations in the upstream reservoir. Both the micro- and nano-PIV techniques should therefore give identical velocity measurements for these flows. Nevertheless, these nPIV data are unique in that they provide a direct experimental verification that the EOF is uniform within 100 nm of the wall, and that $\lambda \ll 100$ nm.

3. Results and discussion

Figure 4 shows a representative nPIV result obtained by averaging velocity data obtained over 1000 consecutive images (i.e. 999 image pairs) from the case shown in the figure 3. The data verify that the flow is essentially uniform in x and z . Results are therefore presented here in terms of the spatially and temporally averaged velocity, or the speed averaged both over the entire field of view and successive pairs of images, respectively. The result is essentially the bulk flow velocity U . Figure 5 compares the values for U from the nPIV measurements as a function of the electric field E for different values of C . The average velocity is linearly proportional to the driving electric field, as expected for constant mobility. The error bars on the nPIV results represent conservative 95% confidence intervals (Kline 1985). These error estimates include both the uncertainty in determining particle displacement in each set of images (calculated using the method of Benedict & Gould 1996) and other experimental uncertainties associated with converting this displacement into actual velocities, such as the estimated physical dimension of one pixel in each image and the CCD camera framing rate.

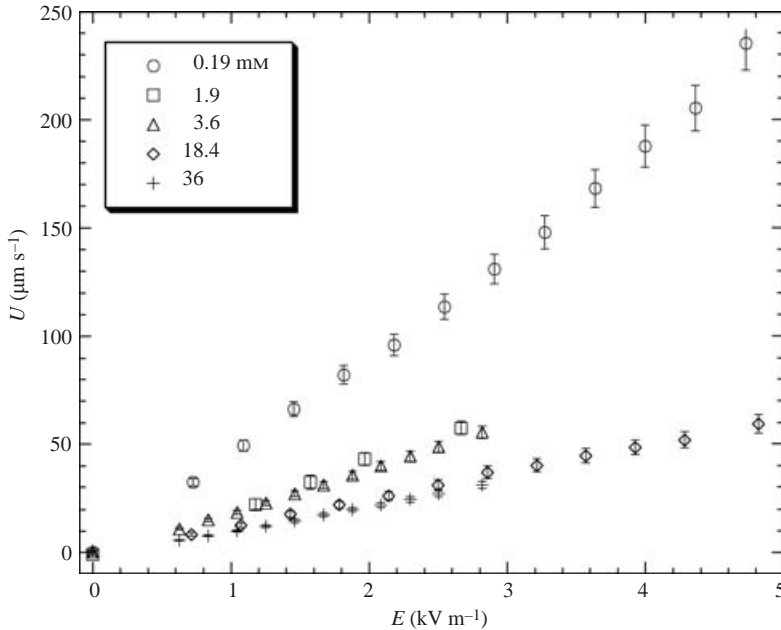


FIGURE 5. Plot of average velocity U as a function of external electric field E for $C = 0.19\text{--}36$ mM sodium tetraborate buffer. The error bars represent 95% confidence intervals.

The biggest physical error (*vs.* experimental errors associated with image acquisition and processing) in the nPIV data is Brownian diffusion of the 100 nm tracers. Out-of-plane Brownian diffusion causes severe ‘particle mismatch,’ where the tracers leave or enter the ~ 100 nm thick region illuminated by the evanescent wave between successive images, reducing the SNR of the cross-correlation peak. For unconfined Brownian motion, the r.m.s. displacement of the particle over the time interval between frames of 6.25 ms is about 240 nm, *vs.* $y_p \approx 100$ nm. Particles within about $0.05D$ of the wall will experience significant lubrication and colloidal forces, and tracers within λ of the wall will sample the very high shear rates ($O(10^3 \text{ s})$) within the EDL. Nevertheless, out-of-plane Brownian fluctuations will ensure that the particles move out of these regions well before lubrication, colloidal and inertial forces have any significant effect upon the particle dynamics. We are currently performing hindered Brownian diffusion simulations to estimate the errors due to this phenomenon.

Errors due to in-plane Brownian diffusion are essentially eliminated by temporally averaging the results in this steady flow. However, the effects of in-plane Brownian diffusion can also be directly estimated from the temporally resolved nPIV results. The standard deviation for a single velocity vector – which reflects the Brownian diffusion averaged over the tracer particles within the interrogation window – at a given location over 999 realizations is typically 15%. After spatial and temporal averaging, this standard deviation accounts for about 25% of the 95% confidence intervals given in figure 5. Experimental errors (due, for example, to the limiting spatial resolution of the CCD camera and errors in determining the magnification) are therefore the dominant source of error in these results.

To further quantify these results, figure 6 compares the experimentally derived mobility μ_{ex} , or the slope of the nPIV data in figure 5, obtained using linear regression

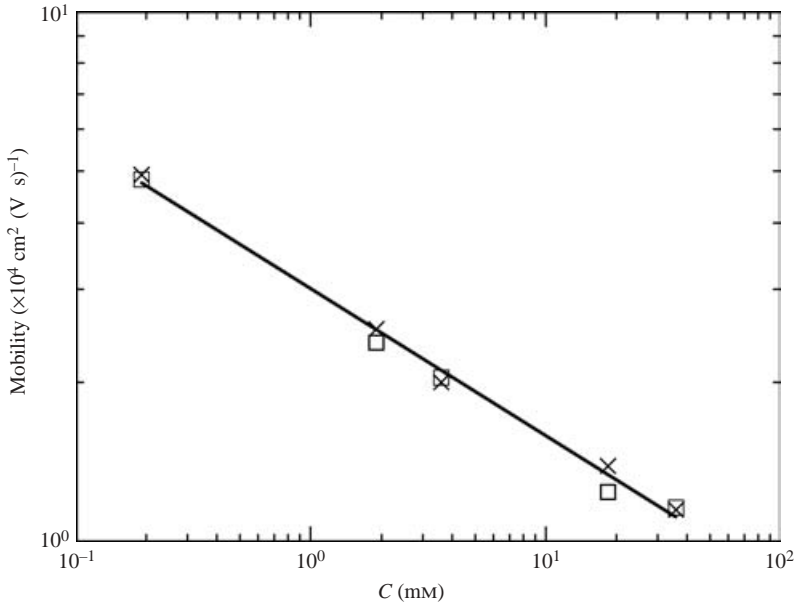


FIGURE 6. Graph of mobility values μ_{ex} (\square) and μ_{eo} (\times) as a function of molar concentration for EOF of sodium tetraborate buffer. The solid line shows equation (3.2) with $\mu_o = 3.00 \times 10^{-4} \text{ cm}^2 (\text{V s})^{-1}$ and $N = 0.277$.

with the electro-osmotic mobility μ_{eo} predicted by an asymptotic model (Conlisk *et al.* 2002):

$$\mu_{eo} = \frac{\epsilon_e \phi_o}{2\mu} \ln \left\{ \frac{g^0}{f^0} \right\}. \tag{3.1}$$

Here, ϵ_e and μ are the electrical permittivity and absolute viscosity, respectively, of the fluid, $\phi_o \equiv RT/F$ (R is the universal ideal gas constant, T the absolute temperature of the fluid and F is Faraday’s constant) is the characteristic scale for the potential, and (g^0, f^0) are the wall mole fractions of the cationic and anionic species, respectively. The experimental and model values for mobility agree within 10% over a 200-fold change in molar concentration, suggesting that the particle tracers follow the flow with good fidelity over the range of E studied. In addition, Ramsey *et al.* (2002) have experimentally measured the mobility of $C = 0.2 \text{ mM}$ sodium tetraborate buffer using a neutral fluorescent molecular (*vs.* particle) tracer and reported $\mu = 4.8 \times 10^{-4} \text{ cm}^2 (\text{V s})^{-1}$ – a value in good agreement with μ_{ex} and μ_{eo} for the $C = 0.19 \text{ mM}$ case. These independent results suggest that particle slip with respect to the fluid (due to electrophoresis) has a negligible effect on mobility for the EOF cases studied here.

Moreover, these experimental and analytical results suggest that the mobility has a power-law scaling with concentration:

$$\mu = \mu_o \left(\frac{C}{1 \text{ mM}} \right)^{-N}. \tag{3.2}$$

A curve-fit of the experimental data points gives $\mu_o = 2.94 \times 10^{-4} \text{ cm}^2 (\text{V s})^{-1}$ and $N = 0.278$. To our knowledge, these are the first results suggesting this scaling, which

cannot be directly derived from the analysis because of the iterative method used to derive f^0 and g^0 .

4. Conclusions

Nanoparticle image velocimetry was used to measure two components of the velocity in fully developed and steady electro-osmotic flow of dilute sodium tetraborate buffer through a rectangular channel with heights in the range 5 – 25 μm within about 100 nm of the channel wall. These are, to our knowledge, the first near-wall velocity field measurements in EOF. These data are also the first experimental verification of analytical predictions that the region of uniform flow extends to within 100 nm of the wall and that the thickness of the EDL in EOF is much less than 100 nm. The mobility of the particle tracers, calculated from spatially and temporally averaged velocity data obtained with this technique, are within 10% of analytical predictions for mobility over a 200-fold change in concentration values. Finally, the results suggest a novel scaling where the mobility is a power-law function of electrolyte concentration.

This work is funded by DARPA DSO under agreement F30602-00-2-0613 by Dr A. Krishnan; we are grateful for their support. We also thank J.P. Alarie, S. Jacobson and J.M. Ramsey of the Laser Spectroscopy and Chemical Microtechnology Group at the Oak Ridge National Laboratories for fabricating the microchannels used in the nPIV measurements and for their advice.

REFERENCES

- AXELROD, D., BURGHARDT, T. P. & THOMPSON, N. L. 1984 Total internal reflection fluorescence. *Annu. Rev. Biophys. Bioengng* **13**, 247–268.
- BENEDICT, L. H. & GOULD, R. D. 1996 Towards better uncertainty estimates for turbulence statistics. *Exps. Fluids* **22**, 129–136.
- BROYLES, B. S., JACOBSON, S. C. & RAMSEY, J. M. 2003 Sample filtration, concentration and separation integrated on microfluidic devices. *Anal. Chem.* **75**, 2761–2767.
- CONLISK, A. T., MCFERRAN, J., ZHENG, Z. & HANSFORD, D. J. 2002 Mass transfer and flow in electrically charged micro- and nano-channels. *Anal. Chem.* **74**, 2139–2150.
- CROCKER, J. C. & GRIER, D. G. 1996 Methods of digital video microscopy for colloidal studies. *J. Colloid Interface Sci.* **179**, 298–310.
- CULBERTSON, C. T., JACOBSON, S. C. & RAMSEY, J. M. 1998 Dispersion sources for compact geometries on microchips. *Anal. Chem.* **70**, 3781–3789.
- CUMMINGS, E. B. 2002 A comparison of theoretical and experimental electrokinetic and dielectrophoretic flow fields. *AIAA Paper* 2002-3193.
- FU, L.-M., LIN, J.-Y. & YANG, R.-J. 2003 Analysis of electroosmotic flow with step change in zeta potential. *J. Colloid Interface Sci.* **258**, 266–275.
- GHOSAL, S. 2002 Lubrication theory for electro-osmotic flow in a microfluidic channel of slowly varying cross-section and wall charge. *J. Fluid Mech.* **459**, 103–128.
- HERR, A. E., MOLHO, J. I., SANTIAGO, J. G., MUNGAL, M. G., KENNY, T. W. & GARGUILO, M. G. 2000 Electroosmotic capillary flow with nonuniform zeta potential. *Anal. Chem.* **72**, 1053–1057.
- HUNTER, R. J. 1981 *Zeta Potential in Colloid Science*. Academic.
- JACOBSON, S. C., HERGENRÖDER, R., KOUTNY, L. B. & RAMSEY, J. M. 1994a High-speed separations on a microchip. *Anal. Chem.* **66**, 1114–1118.
- JACOBSON, S. C., HERGENRÖDER, R., KOUTNY, L. B., WARMACK, R. J. & RAMSEY, J. M. 1994b Effects of injection schemes and column geometry on the performance of microchip electrophoresis devices. *Anal. Chem.* **66**, 1107–1113.
- KEANE, R. D. & ADRIAN, R. J. 1991 Optimization of particle image velocimeters. II. Multiple pulsed systems. *Meas. Sci. Technol.* **2**, 963–974.

- KLINE, S. J. 1985 The purpose of uncertainty analysis. *Trans. ASME J: Fluids Engng* **107**, 153–160.
- LEVINE, S., MARRIOTT, J. R. & ROBINSON, K. 1975 Theory of electrokinetic flow in a narrow parallel-plate channel. *J. Chem. Soc. Faraday Trans. II* **71**, 1–11.
- MEINHART, C. D., WERELEY, S. T. & GRAY, M. H. B. 2000 Volume illumination for two-dimensional particle image velocimetry. *Meas. Sci. Technol.* **11**, 809–814.
- MEINHART, C. D., WERELEY, S. T. & SANTIAGO, J. G. 2000 A PIV algorithm for estimating time-averaged velocity fields. *Trans. ASME J: Fluids Engng* **122**, 285–289.
- PAUL, P. H., GARGUILO, M. G. & RAKESTRAW, R. J. 1998 Imaging of pressure- and electrokinetically driven flows through open capillaries. *Anal. Chem.* **70**, 2459–2467.
- PRIEVE, D. C. & FREJ, N. A. 1990 Total internal reflection microscopy: a quantitative tool for the measurement of colloidal forces. *Langmuir* **6**, 396–403.
- PROBSTEIN, R. F. 1989 *Physicochemical Hydrodynamics*. Butterworths.
- RAMSEY, J. M., ALARIE, J. P., JACOBSON, S. C. & PETERSON, N. J. 2002 Molecular transport through nanometer confined channels. In *Micro Total Analysis Systems 2002* (ed. Y. Baba, S. Shoji & A. van den Berg), p. 314. Kluwer.
- RICE, C. L. & WHITEHEAD, R. 1965 Electrokinetic flow in a narrow capillary. *J. Phys. Chem.* **69**, 4017–4024.
- SANTIAGO, J. G., WERELEY, S. T., MEINHART, C. D., BEEBE, D. J. & ADRIAN, R. J. 1998 A particle image velocimetry system for microfluidics. *Exps. Fluids* **25**, 316–319.
- STONE, S., MEINHART, C. D. & WERELEY, S. T. 2002 Out of plane spatial resolution of volume illumination PIV. *Bull. Am. Phys. Soc.* **47**, 49.
- TRETHERWAY, D. C. & MEINHART, C. D. 2002 Apparent fluid slip at hydrophobic microchannel walls. *Phys. Fluids* **14**, L9–L12.
- VAZQUEZ, M., MCKINLEY, G., MITNIK, L., DESMARAIS, S., MATSUDAIRA, P. & EHRLICH, D. 2002 Electrophoretic injection within microdevices. *Anal. Chem.* **74**, 1952–1961.
- WERELEY, S. T., GUI, L. & MEINHART, C. D. 2002 Advanced algorithms for microscale particle image velocimetry. *AIAA J.* **40**, 1047–1055.
- YANG, C., LI, D. & MASLIYAH, J. H. 1998 Modeling forced liquid convection in rectangular microchannels with electrokinetic effects. *Intl J. Heat Mass Transfer* **41**, 4229–4249.
- ZETTNER, C. M. & YODA, M. 2003 Particle velocity field measurements in a near-wall flow using evanescent wave illumination. *Exps. Fluids* **34**, 115–121.
- ZHENG, Z., HANSFORD, D. & CONLISK, A. T. 2003 Effect of multivalent ions on electroosmotic flow in micro- and nanochannels. *Electrophoresis* **24**, 3006–3017.